

Impact of Structural Polymorphism on Ionic Conductivity in Lithium Copper Pyroborate $\text{Li}_6\text{CuB}_4\text{O}_{10}$

Florian Strauss,^{†,‡,§,∇} Gwenaëlle Rousse,^{‡,§,||,⊥} Daniel Alves Dalla Corte,^{‡,⊥} Carlotta Giacobbe,[#] Robert Dominko,^{†,§} and Jean-Marie Tarascon^{*,‡,§,||,⊥}

[†]National Institute of Chemistry, Hajdrihova 19, SI-1000 Ljubljana, Slovenia

[‡]UMR 8260 “Chimie du Solide et Energie”, Collège de France, 11 Place Marcelin Berthelot, 75231 Paris Cedex 05, France

[§]ALISTORE—European Research Institute, 33 rue Saint-Leu, 80039 Amiens Cedex, France

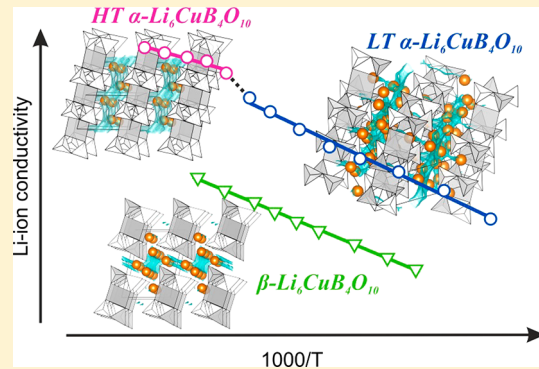
^{||}Sorbonne Université, 4 Place Jussieu, F-75005 Paris, France

[⊥]Réseau sur le Stockage Electrochimique de l’Energie (RS2E), FR CNRS 3459, 80039 Amiens Cedex, France

^{*}ESRF—European Synchrotron Radiation Facility, F-38000 Grenoble, France

Supporting Information

ABSTRACT: The search for high Li-ion conducting ceramics has regained tremendous interest triggered by the renaissance of the all-solid-state battery. Within this context we herein reveal the impact of structural polymorphism of lithium copper pyroborate $\text{Li}_6\text{CuB}_4\text{O}_{10}$ on its ionic conductivity. Using combined *in situ* synchrotron X-ray and neutron powder diffraction, a structural and synthetic relationship between α - and β - $\text{Li}_6\text{CuB}_4\text{O}_{10}$ could be established and its impact on ionic conductivity evolution was followed using electrochemical impedance spectroscopy. We show that the high temperature form of $\text{Li}_6\text{CuB}_4\text{O}_{10}$ exhibits a high Li-ion conductivity (2.7 mS cm^{-1} at 350°C) and solve its crystal structure for the first time. Our results emphasize the significant impact of structural phase transitions on ionic conductivity and show possible high Li-ion mobility within borate based compounds.



INTRODUCTION

Currently, Li-ion batteries (LIBs) relying on liquid organic based electrolytes currently play an important role in powering electric vehicles and portable electronics.¹ However, they are known to approach their limits in terms of energy density, while the demand for high performance energy storage devices is still increasing, mainly driven by the automotive industry. In addition, organic liquid electrolytes in state-of-the-art LIBs are known to present severe safety issues under harsh operating conditions, as well as performance limitations at low or high temperatures.² Continuous research efforts have been made throughout past decades to replace liquid with inorganic solid electrolytes, but a breakthrough came only recently with the discovery of a few highly conducting thiophosphate based ceramics (e.g., $\text{Li}_7\text{P}_2\text{S}_{11}$, $\text{Li}_{10}\text{GeP}_2\text{S}_{12}$),^{3,4} possessing conductivities similar to those of liquid based electrolytes. Subsequently, a rebirth of the all-solid-state battery research took place, and a few additional thiophosphate based compounds showing ionic conductivities in the range 10^{-3} – $10^{-2} \text{ mS cm}^{-1}$ were revealed.^{5,6} Despite their high conductivity, one severe drawback among sulfidic based ion conductors is the release of toxic hydrogen sulfide H_2S upon exposure to ambient atmosphere, requiring strict handling under inert conditions. Accordingly, a lot of research efforts are focused on oxide based solid electrolytes owing to their simple handling and

improved electrochemical stability over sulfide based ion conductors.^{5,7} In particular, borate based compounds are known to form a large variety of anionic networks thanks to the ability of boron to adopt triangular and/or tetrahedral coordinations,^{8,9} which can result in structures providing the possibility to provide pathways for fast ion migration.^{10–12} Indeed, crystalline, as well as amorphous, borate based compounds were reported to possess significant cationic mobility, and moreover, we recently revealed the possible existence of a high temperature form of α - $\text{Li}_6\text{CuB}_4\text{O}_{10}$ showing superionic Li-ion conductivity of 10^{-3} – $10^{-2} \text{ mS cm}^{-1}$ in a temperature range between 350 and 500 °C.¹³ Although it is worth noting that the presence of copper narrows the electrochemical window of this compound, nevertheless this was an impetus for us to embark in a thorough structure–property study among $\text{Li}_6\text{CuB}_4\text{O}_{10}$ species. Moreover, during our investigations we were for the first time able to prepare the second reported polymorph β - $\text{Li}_6\text{CuB}_4\text{O}_{10}$ as a bulk powder. This allowed us to apply differential scanning calorimetry (DSC) combined with *in situ* high temperature synchrotron X-ray and neutron powder diffraction to establish a full structural and synthetic relationship between α - and β - $\text{Li}_6\text{CuB}_4\text{O}_{10}$.

Received: June 28, 2018

Published: August 29, 2018

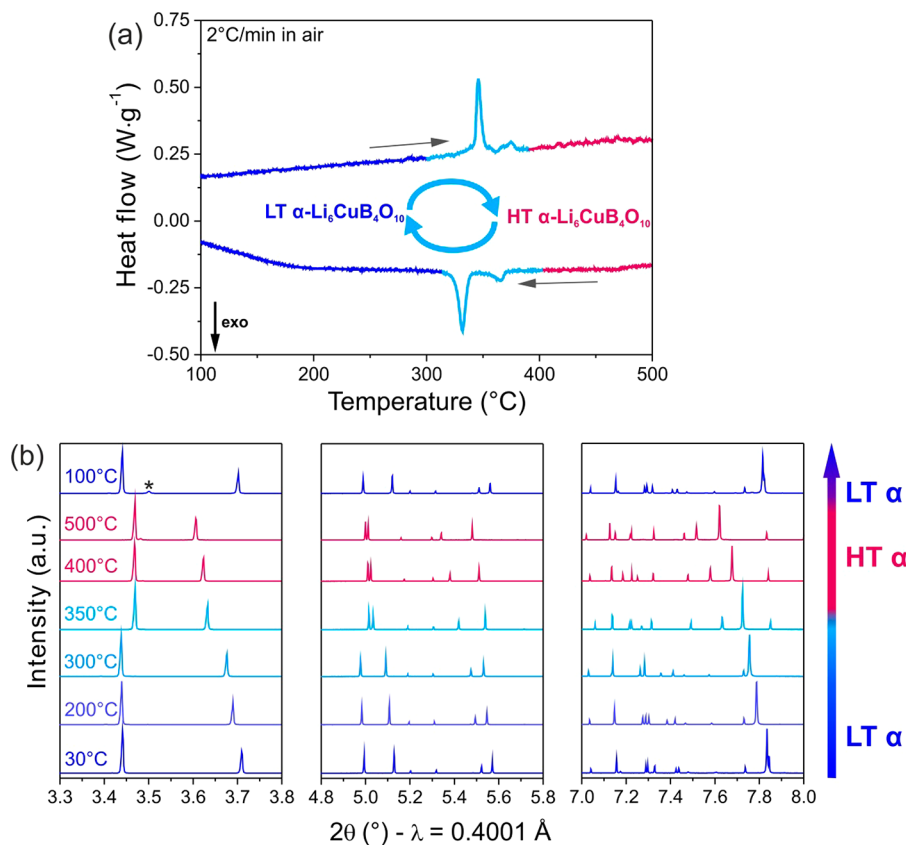


Figure 1. (a) DSC of $\alpha\text{-Li}_6\text{CuB}_4\text{O}_{10}$ during heating/cooling between room temperature and 500 °C. (b) Cutouts of the *in situ* synchrotron XRD pattern recorded at the temperatures as stated in the graphic. The tiny reflection marked with a star corresponds to $\beta\text{-Li}_6\text{CuB}_4\text{O}_{10}$ impurity formed during the high temperature synchrotron measurement.

polymorphs, including a structural determination of the highly conductive high temperature (HT) $\alpha\text{-Li}_6\text{CuB}_4\text{O}_{10}$ polymorph. In addition, the influence of the structural polymorphism on Li-ion conductivity was revealed using electrochemical impedance spectroscopy (EIS) together with bond valence energy (BVEL) calculations.

■ EXPERIMENTAL SECTION

Synthesis. First of all, $\alpha\text{-Li}_6\text{CuB}_4\text{O}_{10}$ was synthesized through mixing stoichiometric amounts of Li_2CO_3 (Sigma-Aldrich, 99%), CuO (Alfa Aesar, 99.7%), and H_3BO_3 (Alfa Aesar, 99+) using a mortar and pestle. The mixture was subsequently heated for 4 h at 450 °C in an alumina crucible in air in order to decompose boric acid. Next, the powder was reground and annealed at 650 °C for 48 h in air, and a royal blue powder was obtained. The $\beta\text{-Li}_6\text{CuB}_4\text{O}_{10}$ was obtained by annealing $\alpha\text{-Li}_6\text{CuB}_4\text{O}_{10}$ powder at 500 °C for at least 9 days in air until the XRD pattern showed a pure phase. Note that for $\beta\text{-Li}_6\text{CuB}_4\text{O}_{10}$ a pale blue color is observed. In order to avoid severe neutron absorption, ^{7}Li and ^{11}B (Sigma-Aldrich, ≥99 at. %) enriched precursors were used for the synthesis of the samples used for neutron diffraction. A similar synthesis protocol as described above was followed.

Physical Characterization. *In situ* high temperature synchrotron X-ray powder diffraction measurements were recorded in Debye–Scherrer geometry at the ID22 beamline at the European Synchrotron Radiation Facility (ESRF, Grenoble, France). The powder sample was placed in a quartz capillary (0.7 mm diameter), and the wavelength was $\lambda = 0.400127 \text{ \AA}$. Measurements were done between room temperature (RT) and 600 °C using a hot air blower (Cyberstar).

Neutron powder diffraction data was recorded on the HRPT high resolution neutron powder diffractometer (Swiss Spallation Neutron Source SINQ, Paul Scherrer Institute) with a constant wavelength of

1.494 Å and a step size of 0.05° in the 2θ range from 3.55° to 164.5° for about 8 h. ^{11}B and ^{7}Li enriched samples were loaded in sealed $\varnothing = 10 \text{ mm}$ vanadium cylindrical cans.

Neutrons and synchrotron X-ray powder patterns were refined using the Rietveld method¹⁴ as implemented in the FullProf program.¹⁵ The peak profile shape was described as a Thomson–Cox–Hastings pseudo-Voigt function. The following parameters were initially refined: (1) scale factor, (2) background coefficients using a Chebyschev function with 24 parameters, (3) peak shape parameters, (4) lattice parameters, (5) fractional atomic coordinates, (6) zero-shift, and (7) isotropic atomic displacement parameters.

Pellets for conductivity measurements were prepared as follows. For $\alpha\text{-Li}_6\text{CuB}_4\text{O}_{10}$, a stoichiometric amount of precursors as described above was first heated for 4 h at 450 °C in air. The mixture was then reground using a mortar and pestle, and approximately 200 mg of the powder was pelletized with approximately 3 tons of pressure within a 13 mm diameter pressing tool and sintered for 48 h at 650 °C in air to obtain $\alpha\text{-Li}_6\text{CuB}_4\text{O}_{10}$ pellets suitable for impedance measurements. Pellets of $\beta\text{-Li}_6\text{CuB}_4\text{O}_{10}$ were obtained by annealing $\alpha\text{-Li}_6\text{CuB}_4\text{O}_{10}$ discs for 9 days at 500 °C in air. To ensure good contact, the top and bottom sides of the pellets were sputtered with gold and placed within a BioLogic MTZ-35 setup equipped with a HTF-1100 furnace. Alternating current (ac) electrochemical impedance measurements (EIS) were carried out in a frequency range from 3.5 MHz to 0.1 Hz applying a 10 mV voltage amplitude. Depressed semicircles derived from impedance spectroscopy were fitted with an $(R_0 - R_1)/\text{CPE}_1$ equivalent circuit, where R_0 represents the initial shift of the impedance arc from zero, R_1 is the sum of grain boundary and bulk resistance, and CPE_1 is a constant phase element. In the case of the absence of a depressed semicircle, the intercept of a linear fit of the Warburg tail with the x -axis was taken as R_1 . Activation energies E_a were calculated from the linear fit of the temperature derived conductivity values using the Arrhenius equation $\sigma T = \sigma_0 \exp(-E_a/$

$k_B T$), where σT ($S \text{ cm}^{-1} \text{ K}$) is the temperature dependent conductivity, σ_0 ($S \text{ cm}^{-1}$) is a pre-exponential factor, and k_B is the Boltzmann constant. Note that pellet porosities ($\sim 70\%$) are not taken into account; thus, underestimated conductivity values can be assumed.

RESULTS AND DISCUSSION

Structural Characterization. Regarding $\text{Li}_6\text{CuB}_4\text{O}_{10}$, three different structural models have been reported in the literature so far, where two of them can be assigned to α - $\text{Li}_6\text{CuB}_4\text{O}_{10}$ and one to β - $\text{Li}_6\text{CuB}_4\text{O}_{10}$. The two structural models reported for α - $\text{Li}_6\text{CuB}_4\text{O}_{10}$ by Pan et al.¹⁶ and Sparta et al.¹⁷ were derived from single crystal XRD, and they reveal a triclinic symmetry with $P\bar{1}$ space group possessing a unit cell volume of $196.79(13)$ and $595.195(1) \text{ \AA}^3$, respectively. Both structural models are closely related, where, in the case of Sparta's cell ($P\bar{1}$), superstructure reflections were taken into account, leading to a tripled unit cell as compared to Pan's structural model. We confirmed Sparta's model on our recently synthesized α - $\text{Li}_6\text{CuB}_4\text{O}_{10}$ phase which shows superstructure reflections.¹³ Turning to the third structural model reported by Kuratieva et al.,¹⁸ it is related to β - $\text{Li}_6\text{CuB}_4\text{O}_{10}$ which crystallizes in a triclinic cell with a $P1$ space group and a unit cell volume of $197.50(4) \text{ \AA}^3$. Such a structure was determined accidentally on a single crystal obtained throughout a synthetic survey of the $\text{Li}_2\text{O}\cdot\text{CuO}\cdot\text{B}_2\text{O}_3$ system, so that neither a structural nor a synthetic relationship could be provided between α - and β - $\text{Li}_6\text{CuB}_4\text{O}_{10}$. Moreover, we recently revealed with this system the existence of a highly Li-ion conducting phase for α - $\text{Li}_6\text{CuB}_4\text{O}_{10}$ above temperatures of 350°C . This finding triggered our interest to fully establish the structural polymorphism among the $\text{Li}_6\text{CuB}_4\text{O}_{10}$ system via high resolution X-ray and neutron powder diffraction coupled with differential scanning calorimetry (DSC) and electrochemical impedance spectroscopy (EIS) with the hope of correlating structure and ionic conducting properties.

DSC was used at first to follow the phase transition upon heating and cooling of α - $\text{Li}_6\text{CuB}_4\text{O}_{10}$ in air at a heating rate of 5°C min^{-1} . As the temperature gradually increases, one can note two subsequent phase transitions between 340 and 380°C with the first one much more pronounced and perfectly reversible upon subsequent cooling of the sample (Figure 1a). To get detailed structural insights into the transitions, high temperature *in situ* synchrotron XRD was performed. As can be seen in Figure 1b on heating a sample of α - $\text{Li}_6\text{CuB}_4\text{O}_{10}$, there is a gradual shift of the reflection until 300°C together with the disappearance of the superstructure reflections located between 5.6° and 6.8° in 2θ (Figure S1). For the pattern recorded at 350°C , one can note an abrupt shift of the main reflections together with the appearance of two new reflections located between 5.6° and 6.8° 2θ which almost fully vanish for temperatures greater than 350°C (Figure S1). This suggests the formation of an intermediate phase around 350°C , as indicated by the two subsequent peaks observed in the DSC trace (Figure 1a). Upon further heating, a gradual shift of the reflections is observed up to 500°C .

At 30°C the XRD patterns can be indexed with the triclinic unit cell in a $P\bar{1}$ space group as reported by Sparta et al.,¹⁷ with lattice parameters $a = 4.82068(1) \text{ \AA}$, $b = 9.23874(1) \text{ \AA}$, $c = 13.96782(1) \text{ \AA}$, $\alpha = 104.35440(5)^\circ$, $\beta = 96.22300(5)^\circ$, and $\gamma = 94.59142(5)^\circ$ leading to a unit cell volume of $595.408(1) \text{ \AA}^3$. Upon further heating up to 350°C , all lattice parameters increase gradually (Figure S2), leading to an overall unit cell

expansion of about 2% to $607.017(1) \text{ \AA}^3$ at 350°C . The absence of superstructure reflections for $T > 350^\circ\text{C}$ suggests a lowering in symmetry or a decrease in the unit cell volume, and thus the possible existence of a high temperature phase of α - $\text{Li}_6\text{CuB}_4\text{O}_{10}$, as recently suggested.¹³ Indeed, a 3 times smaller triclinic unit cell with $P\bar{1}$ space group was sufficient to index the XRD powder patterns for $T > 350^\circ\text{C}$, having unit cell parameters of $a = 4.89603(1) \text{ \AA}$, $b = 6.68944(1) \text{ \AA}$, $c = 6.94800(1) \text{ \AA}$, $\alpha = 84.59495(5)^\circ$, $\beta = 71.99361(5)^\circ$, and $\gamma = 71.83642(5)^\circ$ leading to a unit cell volume of $205.629(1) \text{ \AA}^3$ at 500°C . The cell reported by Pan et al.¹⁶ corresponds therefore to the high temperature form of α - $\text{Li}_6\text{CuB}_4\text{O}_{10}$. A schematic evolution of all lattice parameters is given in Figure S2.

After the sample was cooled to 30°C , all changes observed upon heating in the XRD pattern are perfectly reversible (including the reappearance of superstructure reflections), with the presence of a tiny reflection which can therefore be attributed to the presence of β - $\text{Li}_6\text{CuB}_4\text{O}_{10}$ formed during the measurement (marked with a star in Figure 1b). Together, these results indicate the existence of a temperature-driven phase transition in α - $\text{Li}_6\text{CuB}_4\text{O}_{10}$ with the high temperature (HT) form of α - $\text{Li}_6\text{CuB}_4\text{O}_{10}$ only stable for temperatures above 350°C .

As both HT and LT α - $\text{Li}_6\text{CuB}_4\text{O}_{10}$ contain many light atoms (lithium, boron), the scattering cross sections for X-rays are not sufficient to get detailed structural insights; we thus used neutron powder diffraction (NPD) as a complementary technique to locate them. Isotopically enriched samples (${}^7\text{Li}$, ${}^{11}\text{B}$) were used in order to minimize absorption. The NPD patterns for LT α - $\text{Li}_6\text{CuB}_4\text{O}_{10}$ (recorded at room temperature) and HT α - $\text{Li}_6\text{CuB}_4\text{O}_{10}$ (recorded at 500°C) together with their corresponding Rietveld refinements are shown in Figure 2. Lattice parameters of $a = 4.82299(6) \text{ \AA}$, $b = 9.24126(12) \text{ \AA}$, $c = 13.96993(16) \text{ \AA}$, $\alpha = 104.33028(86)^\circ$, $\beta = 96.21587(92)^\circ$, and $\gamma = 94.58115(102)^\circ$ with an unit cell volume $V = 596.0378(12) \text{ \AA}^3$ were obtained for LT α - $\text{Li}_6\text{CuB}_4\text{O}_{10}$. The HT α - $\text{Li}_6\text{CuB}_4\text{O}_{10}$ polymorphs show lattice parameters of $a = 4.9003(2) \text{ \AA}$, $b = 6.6946(3) \text{ \AA}$, $c = 6.9561(3) \text{ \AA}$, $\alpha = 84.607(3)^\circ$, $\beta = 71.997(3)^\circ$, and $\gamma = 71.842(4)^\circ$, with a unit cell volume of $206.22(2) \text{ \AA}^3$. Those lattice parameters are in full agreement with the one deduced from the synchrotron experiment (Table S1). Moreover, from Fourier difference maps on the LT α pattern, we could locate ${}^7\text{Li}$ positions within the $\text{Cu}(\text{B}_2\text{O}_5)_2$ framework. The same approach was used for the HT β pattern, but only two lithium positions could be obtained with certainty (on general position $2i$ of space group $P\bar{1}$); A third one is indeed expected according to the chemical formula, and our inability to locate it likely comes from its high mobility. Final atomic positions, Wyckoff sites, and isotropic atomic displacement factors are given in Table S2 and Table 1 for the LT and HT α - $\text{Li}_6\text{CuB}_4\text{O}_{10}$ polymorphs, respectively.

The resulting crystal structures are schematically drawn in Figure 3. In LT α - $\text{Li}_6\text{CuB}_4\text{O}_{10}$ copper atoms are distributed over two different crystallographic positions. These copper atoms are 4-fold planar oxygen coordinated by two B_2O_5 groups, forming isolated $\text{Cu}(\text{B}_2\text{O}_5)_2$ units. These units are stacked along the $[12\bar{3}]^*$ direction. Li atoms are distributed in between the $\text{Cu}(\text{B}_2\text{O}_5)_2$ units and are located at the center of the LiO_4 tetrahedron that shares corners and edges (Figure 3a,b). In the case of HT α - $\text{Li}_6\text{CuB}_4\text{O}_{10}$, similar $\text{Cu}(\text{B}_2\text{O}_5)_2$ units are present; however, they are stacked along the $[111]$ direction. Lithium atoms are also in tetrahedral coordination and form pillars along the b -axis (Figure 3c,d). Note that we

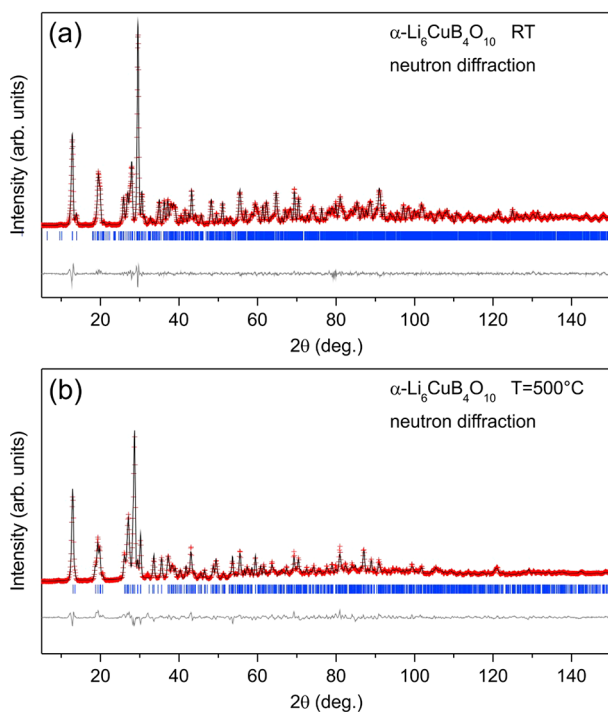


Figure 2. NPD pattern for $\alpha\text{-Li}_6\text{CuB}_4\text{O}_{10}$ recorded at (a) room temperature and (b) 500 °C. Red crosses, black line, blue ticks, and gray continuous line present the observed and calculated data, Bragg reflections, and difference plot, respectively.

were not able to localize the third Li₃ position, indicating high Li-ion mobility.

Throughout our investigation of the $\alpha\text{-Li}_6\text{CuB}_4\text{O}_{10}$ polymorphism, we found out that prolonged annealing of the α -polymorph at temperatures greater than 350 °C triggers a change of the XRD pattern which could be successfully indexed using the structural model for Li₆CuB₄O₁₀ reported by Kuratseva et al.,¹⁸ pertaining to $\beta\text{-Li}_6\text{CuB}_4\text{O}_{10}$. NPD was performed in order to fully confirm the structure of our bulk $\beta\text{-Li}_6\text{CuB}_4\text{O}_{10}$ sample. An isotopically enriched sample (⁷Li, ¹¹B) was also used here to minimize neutron absorption. The corresponding NPD pattern recorded at room temperature is shown in Figure 4. All reflections could be indexed in a triclinic unit cell with P1 space group, and refined lattice parameters are $a = 3.31218(4)$ Å, $b = 6.68272(8)$ Å, $c = 9.27858(11)$ Å, $\alpha = 78.8443(10)$ °, $\beta = 89.7596(11)$ °, and $\gamma = 86.6143(10)$ °

leading to a unit cell volume of 201.14(4) Å³ in good agreement with the data reported in the literature and our synchrotron measurements. Final atomic positions, Wyckoff sites, and isotropic atomic displacement factors are given in Table S3. Last, note that the three crystal structures reported here perfectly match the synchrotron X-ray diffraction patterns, as can be visualized from the Rietveld plots of the LT α , HT α , and $\beta\text{-Li}_6\text{CuB}_4\text{O}_{10}$ polymorphs shown in Figure S3.

The schematic crystal structure of $\beta\text{-Li}_6\text{CuB}_4\text{O}_{10}$ is drawn in Figure 5. It shows the presence of one crystallographic Cu position located at the origin of the unit cell. These Cu atoms are square planar coordinated by two B₂O₅ groups forming Cu(B₂O₅)₂ units which are stacked along the a -axis with Li in tetrahedral coordination sitting in between these units that form a layer along the ab -plane.

Having discovered a synthetic route to prepare bulk samples of $\beta\text{-Li}_6\text{CuB}_4\text{O}_{10}$, we next performed DSC measurements on this phase by heating it at a rate of 5 °C min⁻¹ until 650 °C. The corresponding heating and cooling traces are shown in Figure 6a. Note the appearance upon heating of a broad peak between 550 and 600 °C and of a tiny peak between 300 and 350 °C on subsequent cooling of the sample. *In situ* synchrotron XRD was then used to identify the nature of these changes (Figure 6b). For XRD patterns recorded up to 500 °C, one can note a gradual shift of all reflections leading to an increase in lattice parameters (Figure S3) as well as in the unit cell parameter that reaches 200.709 Å³ at 500 °C (Figure S5). If the temperature is further raised to 550 °C, reflections which can be attributed to HT $\alpha\text{-Li}_6\text{CuB}_4\text{O}_{10}$ appear, hence leading to a biphasic domain. However, for temperatures above 600 °C the phase change from $\beta\text{-Li}_6\text{CuB}_4\text{O}_{10}$ to HT $\alpha\text{-Li}_6\text{CuB}_4\text{O}_{10}$ is complete. After subsequent cooling to room temperature, the corresponding XRD pattern can be perfectly indexed with the LT $\alpha\text{-Li}_6\text{CuB}_4\text{O}_{10}$ (including the presence of superstructure reflections), hence implying that the small peak in the DSC curve between 340 and 380 °C can be correlated to the HT → LT $\alpha\text{-Li}_6\text{CuB}_4\text{O}_{10}$ transition, as already shown above (Figure 1a).

We can now recap our observations and establish a complete overview of the structural polymorphism in Li₆CuB₄O₁₀. The corresponding crystal structures, synthetic pathways, and schematic energy pathways are shown in Figure 7. Owing to the close structural similarities between all three polymorphs, with the exception of a different reordering of Li positions in between the Cu(B₂O₅)₂ units, it is not obvious to identify what

Table 1. Structural Parameters of HT $\alpha\text{-Li}_6\text{CuB}_4\text{O}_{10}$ Determined from the Rietveld Refinement of the NPD Data^a

atom	Wyckoff site	x	y	z	B (Å ²)
Cu1	1a	0	0	0	3.5(3)
B1	2i	0.3713(16)	0.2162(11)	0.2287(11)	0.88(13)
B2	2i	0.544(2)	0.2944(14)	0.8474(14)	2.5(2)
O1	2i	0.359(3)	0.8637(18)	0.7648(18)	4.6(3)
O2	2i	0.164(3)	0.7995(19)	0.170(2)	5.2(3)
O3	2i	0.313(2)	0.2741(14)	0.0419(15)	3.0(2)
O4	2i	0.143(2)	0.2480(16)	0.3931(16)	2.73(19)
O5	2i	0.431(3)	0.3864(15)	0.6892(18)	3.8(3)
Li1	2i	0.171(6)	0.203(4)	0.635(4)	3.8(3)
Li2	2i	0.261(7)	0.649(5)	0.553(5)	3.9(7)
Li3	undetermined	undetermined	undetermined	undetermined	undetermined

^aHT $\alpha\text{-Li}_6\text{CuB}_4\text{O}_{10}$: $V = 206.22(2)$ Å³, $P\bar{1}$ space group, $Z = 1$, $a = 4.9003(2)$ Å, $b = 6.6946(3)$ Å, $c = 6.9561(3)$ Å, $\alpha = 84.607(3)$ °, $\beta = 71.997(3)$ °, $\gamma = 71.842(4)$ °, density = 2.372 g cm⁻³, $R_{\text{Bragg}} = 8.33\%$, $\chi^2 = 16.2$.

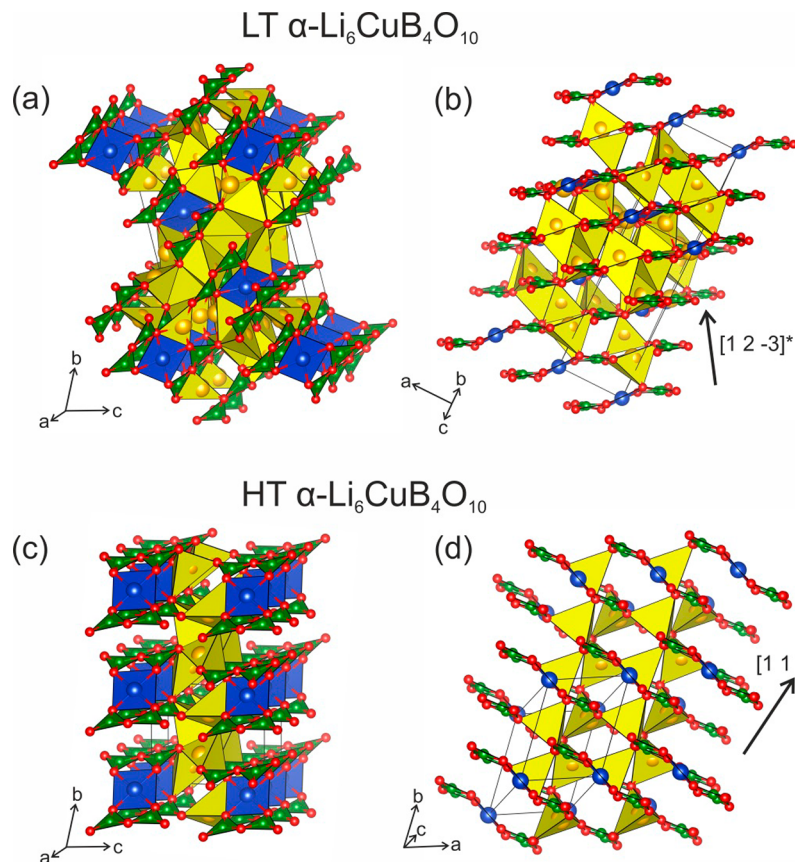


Figure 3. Structure of (a, b) LT $\alpha\text{-Li}_6\text{CuB}_4\text{O}_{10}$ and (c, d) HT $\alpha\text{-Li}_6\text{CuB}_4\text{O}_{10}$ along different crystallographic directions. Lithium, boron, copper, and oxygen are drawn in yellow, green, blue, and red, respectively.

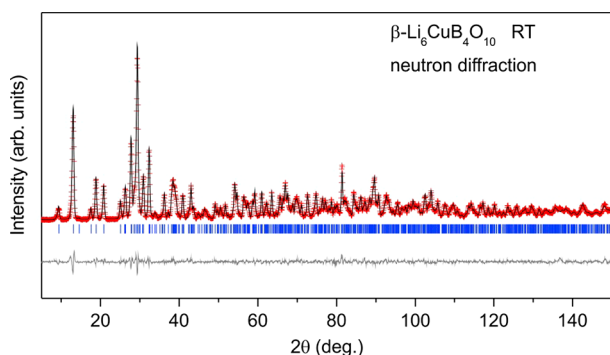


Figure 4. NPD pattern for $\beta\text{-Li}_6\text{CuB}_4\text{O}_{10}$ recorded at room temperature. Red crosses, black line, blue ticks, and gray continuous line present the observed and calculated data, Bragg reflections, and difference plot, respectively.

stabilizes one over the other. The synthesis path is equally complex. Starting from a stoichiometric mixture of $3\text{Li}_2\text{O}\cdot\text{CuO}\cdot 2\text{B}_2\text{O}_3$, one would expect the HT $\alpha\text{-Li}_6\text{CuB}_4\text{O}_{10}$ phase to form at high temperatures, but it is not as simple. Indeed, we found that if the annealing time is rather short, the LT $\alpha\text{-Li}_6\text{CuB}_4\text{O}_{10}$ phase is obtained upon cooling. Moreover, as experimentally observed, the transition between LT and HT $\alpha\text{-Li}_6\text{CuB}_4\text{O}_{10}$ is fast in both directions and perfectly reversible, implying small kinetic barriers and therefore the metastable nature of the HT $\alpha\text{-Li}_6\text{CuB}_4\text{O}_{10}$ phase. It then does not come as a surprise that all attempts to stabilize the HT $\alpha\text{-Li}_6\text{CuB}_4\text{O}_{10}$ structure at RT through quenching samples in liquid nitrogen or isovalent doping (Zn^{2+} , Mg^{2+} , Ca^{2+}) were not successful

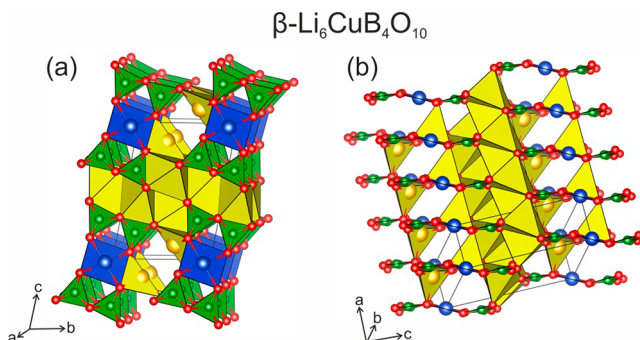


Figure 5. Structure of $\beta\text{-Li}_6\text{CuB}_4\text{O}_{10}$ along different crystallographic directions. Lithium, boron, copper, and oxygen are drawn in yellow, green, blue, and red, respectively.

(Figure 7b). However, if HT $\alpha\text{-Li}_6\text{CuB}_4\text{O}_{10}$ is kept for a long time at sufficient high temperatures ($\sim 500^\circ\text{C}$), it transforms further into $\beta\text{-Li}_6\text{CuB}_4\text{O}_{10}$, whose formation seems to be kinetically hindered but thermodynamically favored. A possible reason might be that, during the HT α to β transformation, two subsequent energy barriers need to be overcome, possibly pertaining to the rearrangement of the $\text{Cu}(\text{B}_2\text{O}_5)_2$ units and relocalization of the Li³ position. In contrast we found the reverse phase transition $\beta \rightarrow \text{LT } \alpha$ to be quite rapid as it only requires a short period of time (a few hours) at temperatures $> 550^\circ\text{C}$.

Li-Ion Mobility. With the complex structural polymorphism in $\text{Li}_6\text{CuB}_4\text{O}_{10}$ being established, we now investigate its impact on Li-ion mobility by first highlighting the migration

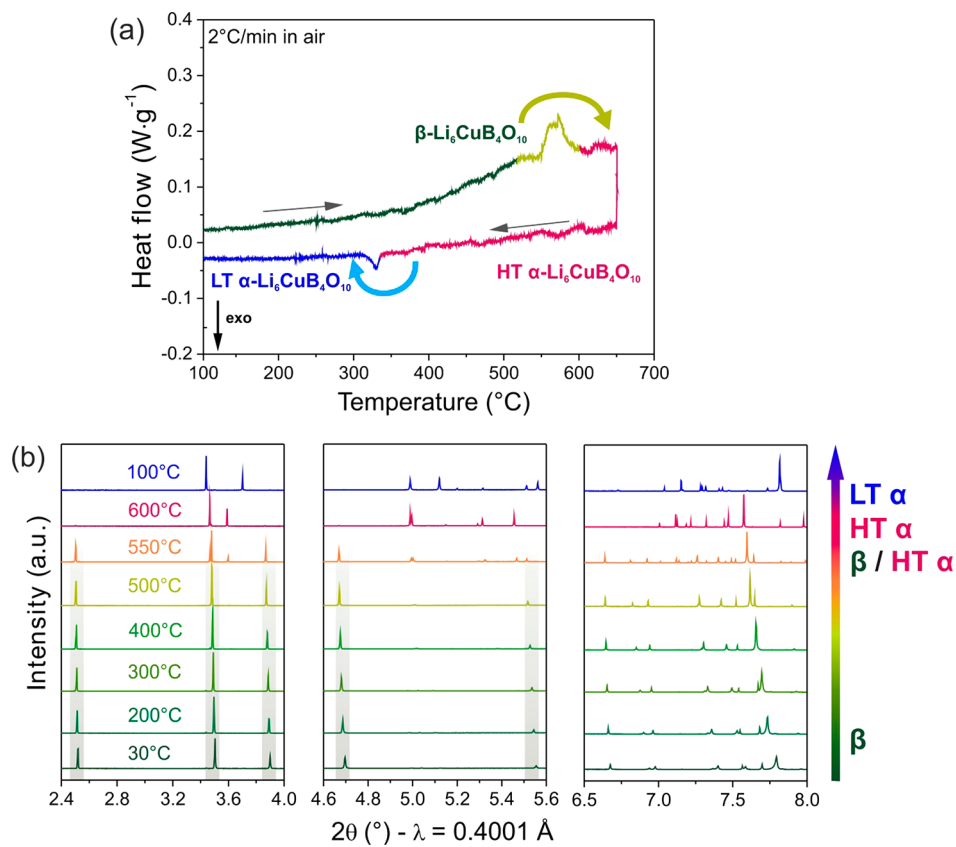


Figure 6. (a) DSC of $\beta\text{-Li}_6\text{CuB}_4\text{O}_{10}$ during heating/cooling between room temperature and 650 °C. (b) Cutouts of the *in situ* synchrotron XRD pattern recorded at the temperatures as stated in the graphic. Gray bars indicate reflections of $\beta\text{-Li}_6\text{CuB}_4\text{O}_{10}$.

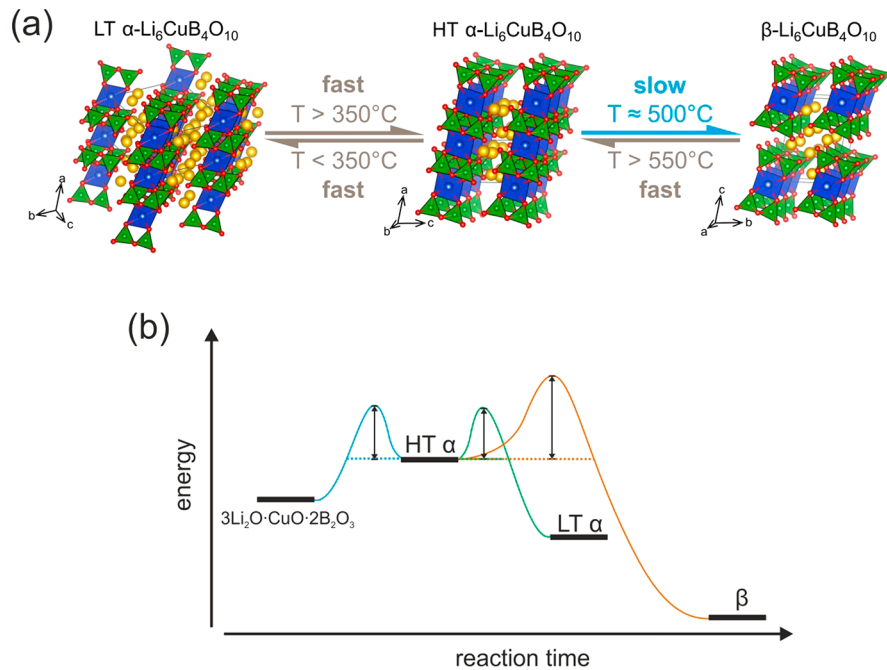


Figure 7. (a) Overview of the complete structural polymorphism in $\text{Li}_6\text{CuB}_4\text{O}_{10}$ involving LT and HT α -phase, as well as a β -phase. Lithium, boron, copper, and oxygen are drawn in yellow, green, blue, and red, respectively. (b) Schematic representation of the reaction pathways for the different polymorphs.

pathways for Li-ions in the various polymorphs as deduced through bond valence energy landscapes (BVELs) calculations. Energies 1.0 eV above the minimum energy (E_{plot}) were chosen for all $\text{Li}_6\text{CuB}_4\text{O}_{10}$ polymorphs in order to yield

comparable BVEL maps. As shown in Figure 8a, for LT $\alpha\text{-Li}_6\text{CuB}_4\text{O}_{10}$ a 3D diffusion network is visible involving all Li positions, suggesting feasible Li-ion mobility. Going to HT $\alpha\text{-Li}_6\text{CuB}_4\text{O}_{10}$ (Figure 8b), 3D Li-ion percolation pathways

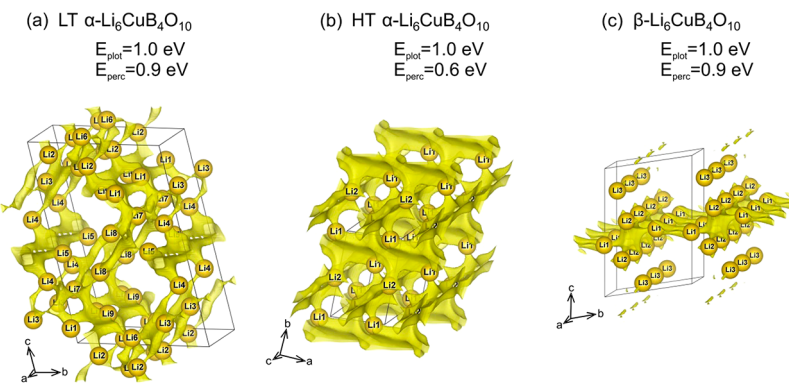


Figure 8. BVELs of LT α -, HT α -, and β - $\text{Li}_6\text{CuB}_4\text{O}_{10}$. Yellow spheres indicate Li atoms, and yellow domains represent migration pathways for Li-ions in the structure at 1.0 eV above the minimum energy. The corresponding percolation energies for Li-ion migration for each polymorph are also given in the graphic.

involving all the atoms are also obtained from BVEL calculations, with therefore a difference nested in Li atoms which are now statistically distributed over many more positions compared to LT α - $\text{Li}_6\text{CuB}_4\text{O}_{10}$. This results in much broader diffusion pathways, thus indicating high Li-ion mobility along with decreased Li-ion migration barriers. This is in line with the percolation energy (E_{perc}) which is 0.9 eV in the case of LT α - and β - $\text{Li}_6\text{CuB}_4\text{O}_{10}$ in contrast to 0.6 eV for HT α - $\text{Li}_6\text{CuB}_4\text{O}_{10}$. Note that this elevated Li-ion mobility was already suggested by the inability to localize Li3 through NPD. In contrast for β - $\text{Li}_6\text{CuB}_4\text{O}_{10}$, only Li1 and Li2 are participating in Li migration, leading to 2D conduction pathways along the ab -plane (Figure 8c), implying the lowest Li-ion mobility among the $\text{Li}_6\text{CuB}_4\text{O}_{10}$ polymorphs.

To support our BVEL calculations, ac impedance spectroscopy was conducted on sintered pellets for LT α -, HT α -, and β - $\text{Li}_6\text{CuB}_4\text{O}_{10}$ for temperatures between 130 and 350 °C, 350 and 500 °C, and 170 and 400 °C, respectively. Corresponding ac impedance plots are shown in Figure S6. The data for LT α - $\text{Li}_6\text{CuB}_4\text{O}_{10}$ recorded at 184 °C is characterized as a depressed semicircle with a Warburg diffusion tail. One equivalent circuit (R/CPE) was used to fit the data, thus preventing differentiation between bulk and grain boundary contributions. If the temperature is further increased above the structural LT $\alpha \rightarrow$ HT α transition, the semicircle fully disappears and only a Warburg tail is present, suggesting a sharp increase in ionic conductivity before and after the transition. In the case of β - $\text{Li}_6\text{CuB}_4\text{O}_{10}$, a depressed semicircle with a Warburg tail (Figure S6) is present over the whole measured temperature range. The data was fitted using the same methodology as described above. On the basis of the temperature dependent resistances obtained from ac impedance spectroscopy, the ionic conductivity and corresponding activation energies were calculated. For LT α - $\text{Li}_6\text{CuB}_4\text{O}_{10}$, a linear increase in conductivity can be observed reaching $3.9 \times 10^{-4} \text{ S cm}^{-1}$ at 320 °C correlated to an activation energy of 1.07 eV. For temperatures greater than 350 °C, the structural transition LT $\alpha \rightarrow$ HT α causes a sharp rise in conductivity reaching $2.7 \times 10^{-3} \text{ S cm}^{-1}$ at 350 °C and a lowering in activation energy by ~50% leading to 0.52 eV. Turning to β - $\text{Li}_6\text{CuB}_4\text{O}_{10}$, a linear increase in conductivity is observed over the entire temperature range, reaching $7.8 \times 10^{-7} \text{ S cm}^{-1}$ at 390 °C associated with an activation energy of 0.92 eV. In order to separate ionic from electronic contributions to the conductivity, additional dc polarization measurements were conducted using the same

setup as for ac impedance spectroscopy (ion blocking electrodes), but applying a dc voltage of 1 V and following the current response. Usually, after a fast decay, a steady-state region is reached, from which the electronic resistance was calculated using Ohm's law (Figure S7). On the basis of these values, the corresponding partial electronic conductivity was calculated, and the activation energy was determined from the corresponding Arrhenius plot (Figure S8). For α - $\text{Li}_6\text{CuB}_4\text{O}_{10}$ the electronic conductivity increases linearly from 2.3×10^{-7} to $1.1 \times 10^{-6} \text{ S cm}^{-1}$ as the temperature is increased from 172 to 495 °C, and this gives an activation energy of 0.17 eV (Figure 9). This small increase contrasts significantly with the

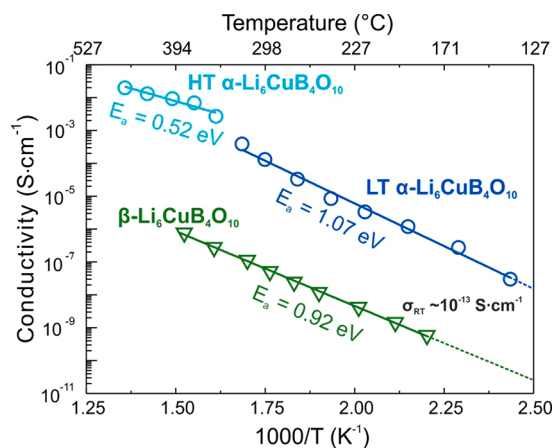


Figure 9. Arrhenius plot of the ac conductivity for LT α -, HT α -, and β - $\text{Li}_6\text{CuB}_4\text{O}_{10}$.

strong increase in conductivity obtained from impedance spectroscopy, thus indicating the predominance of the ionic conductivity to the overall sample conductivity. Last, the β - $\text{Li}_6\text{CuB}_4\text{O}_{10}$ equally reflects a linear increase in electronic conductivity from 5.9×10^{-10} to $1.1 \times 10^{-8} \text{ S cm}^{-1}$ between 237 and 394 °C, respectively, along with an activation energy of 0.57 eV. As the increase of about 2 orders of magnitude in electronic conductivity is comparable to the increase in conductivity derived from the impedance measurements, this suggests both electronic, as well as ionic, transport being present in β - $\text{Li}_6\text{CuB}_4\text{O}_{10}$ which appears to behave as a mixed conductor.

CONCLUSION

In summary, we have thoroughly investigated the relationship of structural polymorphism–ionic conductivity in the $\text{Li}_6\text{CuB}_4\text{O}_{10}$ system. Combined *in situ* synchrotron X-ray and neutron powder diffraction measurements complemented with DSC analysis allowed us to reveal structural and synthetic relations among the three different polymorphs, pertaining to LT and HT forms of $\alpha\text{-Li}_6\text{CuB}_4\text{O}_{10}$ and $\beta\text{-Li}_6\text{CuB}_4\text{O}_{10}$. For temperatures above 350 °C, LT $\alpha\text{-Li}_6\text{CuB}_4\text{O}_{10}$ transforms into HT $\alpha\text{-Li}_6\text{CuB}_4\text{O}_{10}$, whose crystal structure was solved for the first time, and we show that one Li atom among three Li positions cannot be localized, indicating a high Li-ion mobility. This was confirmed by the appearance of a drastic jump in ionic conductivity (2.7 mS cm⁻¹ at 350 °C) after the LT $\alpha \rightarrow \text{HT } \alpha$ transition for temperatures. Moreover, we show that it is possible to prepare bulk powder $\beta\text{-Li}_6\text{CuB}_4\text{O}_{10}$, and not only single crystals, through annealing $\alpha\text{-Li}_6\text{CuB}_4\text{O}_{10}$ for at least 9 days at 500 °C. The as-obtained $\beta\text{-Li}_6\text{CuB}_4\text{O}_{10}$ transforms back into $\alpha\text{-Li}_6\text{CuB}_4\text{O}_{10}$ if heated to temperatures greater than 550 °C. Nevertheless, $\beta\text{-Li}_6\text{CuB}_4\text{O}_{10}$ shows a substantial lower ionic conductivity compared to that of the α -polymorph, most likely related to anisotropic Li conduction pathways.

Generally speaking, the rather poor ionic conductivity observed for low temperature $\text{Li}_6\text{CuB}_4\text{O}_{10}$ (LT α - and β -polymorph) is most likely rooted in defect-driven ion conduction and is associated with a high energy barrier for ion migration (~1 eV). In contrast, for HT $\alpha\text{-Li}_6\text{CuB}_4\text{O}_{10}$, the ionic conduction is most likely nested in a structural disorder effect as suggested by our inability to locate the Li3 position. Such an order-disorder phase transition (LT $\alpha \rightarrow \text{HT } \alpha$) improves ionic conductivity by one order of magnitude while lowering the activation energy barrier as has been observed for a large variety of Li/Na-ion conductors.^{19–22} The ionic conductivity of the HT $\alpha\text{-Li}_6\text{CuB}_4\text{O}_{10}$ phase for $T \geq 350$ °C is comparable to state-of-the-art garnet based Li-ion conductors (~10⁻³ S/cm for cubic $\text{Li}_7\text{La}_3\text{Zr}_2\text{O}_{12}$), with the latter therefore at room temperature. Nevertheless, in the case of garnet type ion conductors, the highly conductive cubic phase, usually present at elevated temperatures, could be stabilized at room temperature through aliovalent doping,^{7,23} which we have found is not possible for HT $\alpha\text{-Li}_6\text{CuB}_4\text{O}_{10}$ as described in the text.

Despite such findings, the values of ionic conductivity, in particular at room temperature, are far too low to be considered for practical applications in all-solid-state batteries, and furthermore, the presence of a Cu redox center narrows the electrochemical stability window (similar potential window for α - and $\beta\text{-Li}_6\text{CuB}_4\text{O}_{10}$).¹³ Nevertheless, our results highlight the strong influence of minimal structural changes on cation mobility in borate based compounds, hopefully triggering further explorative research toward borate based ion conductors for Li/Na ion batteries.

ASSOCIATED CONTENT

Supporting Information

The Supporting Information is available free of charge on the ACS Publications website at DOI: [10.1021/acs.inorgchem.8b01785](https://doi.org/10.1021/acs.inorgchem.8b01785).

Crystallographic data for LT $\alpha\text{-Li}_6\text{CuB}_4\text{O}_{10}$ and $\beta\text{-Li}_6\text{CuB}_4\text{O}_{10}$, cutout of the *in situ* synchrotron XRD patterns for $\alpha\text{-Li}_6\text{CuB}_4\text{O}_{10}$ during heating and cooling, evolution of lattice parameters for α - and $\beta\text{-Li}_6\text{CuB}_4\text{O}_{10}$

and representative ac impedance plots, and dc polarization measurements and Arrhenius plot for electronic conductivity ([PDF](#))

AUTHOR INFORMATION

Corresponding Author

*E-mail: jean-marie.tarascon@college-de-france.fr.

ORCID

Florian Strauss: [0000-0001-5817-6349](https://orcid.org/0000-0001-5817-6349)

Gwenaëlle Rousse: [0000-0001-8877-0015](https://orcid.org/0000-0001-8877-0015)

Robert Dominko: [0000-0002-6673-4459](https://orcid.org/0000-0002-6673-4459)

Present Address

^VBattery and Electrochemistry Laboratory (BELLA), Institute of Nanotechnology (INT), Karlsruhe Institute of Technology (KIT), Hermann-von-Helmholtz-Platz 1, D-76344 Eggenstein-Leopoldshafen, Germany

Notes

The authors declare no competing financial interest.

ACKNOWLEDGMENTS

F.S. acknowledges ALISTORE-ERI for his Ph.D. grant. The authors thank Vladimir Pomjakushin (SINQ, Paul Scherrer Institute, Villigen, Switzerland) for assistance with the neutron powder diffraction measurements. Matthieu Courty (LRCS, Amiens, France) is acknowledged for TGA-DSC measurements.

REFERENCES

- (1) Larcher, D.; Tarascon, J.-M. Towards Greener and More Sustainable Batteries for Electrical Energy Storage. *Nat. Chem.* **2015**, *7* (1), 19–29.
- (2) Liu, W.; Oh, P.; Liu, X.; Lee, M.-J.; Cho, W.; Chae, S.; Kim, Y.; Cho, J. Nickel-Rich Layered Lithium Transition-Metal Oxide for High-Energy Lithium-Ion Batteries. *Angew. Chem., Int. Ed.* **2015**, *54* (15), 4440–4457.
- (3) Yamane, H.; Shibata, M.; Shimane, Y.; Junke, T.; Seino, Y.; Adams, S.; Minami, K.; Hayashi, A.; Tatsumisago, M. Crystal Structure of a Superionic Conductor, $\text{Li}_7\text{P}_3\text{S}_{11}$. *Solid State Ionics* **2007**, *178* (15–18), 1163–1167.
- (4) Kamaya, N.; Homma, K.; Yamakawa, Y.; Hirayama, M.; Kanno, R.; Yonemura, M.; Kamiyama, T.; Kato, Y.; Hama, S.; Kawamoto, K.; et al. A Lithium Superionic Conductor. *Nat. Mater.* **2011**, *10* (9), 682–686.
- (5) Bachman, J. C.; Muy, S.; Grimaud, A.; Chang, H.-H.; Pour, N.; Lux, S. F.; Paschos, O.; Maglia, F.; Lupart, S.; Lamp, P.; et al. Inorganic Solid-State Electrolytes for Lithium Batteries: Mechanisms and Properties Governing Ion Conduction. *Chem. Rev.* **2016**, *116* (1), 140–162.
- (6) Kato, Y.; Hori, S.; Saito, T.; Suzuki, K.; Hirayama, M.; Mitsui, A.; Yonemura, M.; Iba, H.; Kanno, R. High-Power All-Solid-State Batteries Using Sulfide Superionic Conductors. *Nat. Energy* **2016**, *1* (4), 16030.
- (7) Thangadurai, V.; Narayanan, S.; Pinzar, D. Garnet-Type Solid-State Fast Li Ion Conductors for Li Batteries: Critical Review. *Chem. Soc. Rev.* **2014**, *43* (13), 4714.
- (8) Rousse, G.; Baptiste, B.; Lelong, G. Crystal Structures of $\text{Li}_6\text{B}_4\text{O}_9$ and $\text{Li}_3\text{B}_{11}\text{O}_{18}$ and Application of the Dimensional Reduction Formalism to Lithium Borates. *Inorg. Chem.* **2014**, *53* (12), 6034–6041.
- (9) Heller, G. A Survey of Structural Types of Borates and Polyborates. In *Structural Chemistry of Boron and Silicon*; Springer, 1986; pp 39–98.
- (10) Mehrer, H.; Imre, A. W.; Tanguep-Nijocep, E. Diffusion and Ionic Conduction in Oxide Glasses. *J. Phys. Conf. Ser.* **2008**, *106*, 012001.

- (11) Tuller, H. L.; Button, D. P.; Uhlmann, D. R. Fast Ion Transport in Oxide Glasses. *J. Non-Cryst. Solids* **1980**, *40* (1–3), 93–118.
- (12) Rowsell, J. L.C.; Taylor, N. J.; Nazar, L. F. Structure and Ion Exchange Properties of a New Cobalt Borate with a Tunnel Structure “Templated” by Na^+ . *J. Am. Chem. Soc.* **2002**, *124* (23), 6522–6523.
- (13) Strauss, F.; Rousse, G.; Alves Dalla Corte, D.; Ben Hassine, M.; Saubanère, M.; Tang, M.; Vezin, H.; Courty, M.; Dominko, R.; Tarascon, J.-M. Electrochemical Activity and High Ionic Conductivity of Lithium Copper Pyroborate $\text{Li}_6\text{CuB}_4\text{O}_{10}$. *Phys. Chem. Chem. Phys.* **2016**, *18* (22), 14960–14969.
- (14) Rietveld, H. A Profile Refinement Method for Nuclear and Magnetic Structures. *J. Appl. Crystallogr.* **1969**, *2* (2), 65–71.
- (15) Rodríguez-Carvajal, J. Recent Advances in Magnetic Structure Determination by Neutron Powder Diffraction. *Phys. B* **1993**, *192* (1–2), 55–69.
- (16) Pan, S.; Smit, J. P.; Watkins, B.; Marvel, M. R.; Stern, C. L.; Poepelmeier, K. R. Synthesis, Crystal Structure, and Nonlinear Optical Properties of $\text{Li}_6\text{CuB}_4\text{O}_{10}$: A Congruently Melting Compound with Isolated $[\text{CuB}_4\text{O}_{10}]^{6-}$ Units. *J. Am. Chem. Soc.* **2006**, *128* (35), 11631–11634.
- (17) Sparta, K. Structural Investigation of Quaternary Copper Oxides with Low Dimensional Magnetic Properties. Ph.D. Thesis, Institut für Kristallographie of the RWTH-Aachen, Aachen, Germany, 2003.
- (18) Kuratjeva, N. V.; Bánki, M.; Tsirlin, A. A.; Eckert, J.; Ehrenberg, H.; Mikhailova, D. New Lithium Copper Borates with BO_3 Triangles: $\text{Li}_6\text{CuB}_4\text{O}_{10}\text{Li}_3\text{CuB}_3\text{O}_7\text{Li}_8\text{Cu}_7\text{B}_{14}\text{O}_{32}$ and $\text{Li}_2\text{Cu}_9\text{B}_{12}\text{O}_{28}$. *Inorg. Chem.* **2013**, *52* (24), 13974–13983.
- (19) Saha, S.; Rousse, G.; Alcover, I. B.; Courty, M.; Dalla Corte, D. A.; Tarascon, J.-M. Polymorphism in $\text{Li}_4\text{Zn}(\text{PO}_4)_2$ and Stabilization of Its Structural Disorder to Improve Ionic Conductivity. *Chem. Mater.* **2018**, *30* (4), 1379–1390.
- (20) Harada, Y.; Hirakoso, Y.; Kawai, H.; Kuwano, J. Order–disorder of the A-Site Ions and Lithium Ion Conductivity in the Perovskite Solid Solution $\text{La}_{0.67-x}\text{Li}_{3x}\text{TiO}_3$ ($X=0.11$). *Solid State Ionics* **1999**, *121* (1–4), 245–251.
- (21) Tang, W. S.; Dimitrieva, M.; Stavila, V.; Zhou, W.; Wu, H.; Talin, A. A.; Udovic, T. J. Order–Disorder Transitions and Superionic Conductivity in the Sodium *Nido*-Undeca(carba)borates. *Chem. Mater.* **2017**, *29* (24), 10496–10509.
- (22) Wang, X. P.; Xia, Y.; Hu, J.; Xia, Y. P.; Zhuang, Z.; Guo, L. J.; Lu, H.; Zhang, T.; Fang, Q. F. Phase Transition and Conductivity Improvement of Tetragonal Fast Lithium Ionic Electrolyte $\text{Li}_7\text{La}_3\text{Zr}_2\text{O}_{12}$. *Solid State Ionics* **2013**, *253*, 137–142.
- (23) Cussen, E. J. Structure and Ionic Conductivity in Lithium Garnets. *J. Mater. Chem.* **2010**, *20* (25), 5167.